Multi-Atlas Segmentation and Spatial Alignment of the Human Embryo in First Trimester 3D Ultrasound

Wietske A.P. Bastiaansen

w.bastiaansen@erasmusmc.nl

Biomedical Imaging Group Rotterdam, Department of Radiology and Nuclear Medicine, Erasmus MC, University Medical Center Rotterdam, The Netherlands

Department of Obstetrics and Gynaecology, Erasmus MC, University Medical Center Rotterdam, The Netherlands

Melek Rousian

Department of Obstetrics and Gynaecology, Erasmus MC, University Medical Center Rotterdam, The Netherlands

Régine P.M. Steegers-Theunissen

Department of Obstetrics and Gynaecology, Erasmus MC, University Medical Center Rotterdam, The Netherlands

Wiro J. Niessen

Biomedical Imaging Group Rotterdam, Department of Radiology and Nuclear Medicine, Erasmus MC, University Medical Center Rotterdam, The Netherlands

Faculty of Applied Sciences, Delft University of Technology, The Netherlands

Anton H.J. Koning

Generation R Study Group, Erasmus MC, University Medical Center, Rotterdam, The Netherlands

Stefan Klein

Biomedical Imaging Group Rotterdam, Department of Radiology and Nuclear Medicine, Erasmus MC, Rotterdam, University Medical Center, The Netherlands

Abstract

Segmentation and spatial alignment of ultrasound imaging data acquired in the in first trimester are crucial for monitoring early human embryonic growth and development throughout this crucial period of life. Current approaches are either manual or semi-automatic and are therefore very time-consuming and prone to errors. To automate these tasks, we propose a multi-atlas framework for automatic segmentation and spatial alignment of the embryo using deep learning with minimal supervision. Our framework learns to register the embryo to an atlas, which consists of the ultrasound images acquired at a range of gestational ages, segmented and spatially aligned to a predefined standard orientation. From this, we can derive the segmentation of the embryo and put the embryo in standard orientation. Ultrasound images acquired at 8+0 till 12+6 weeks gestational age were used and eight pregnancies were selected as atlas images. We evaluated different fusion strategies to incorporate multiple atlases: 1) training the framework using atlas images from a single pregnancy, 2) training the framework with data of all available atlases and 3) ensembling of the frameworks trained per pregnancy. To evaluate the performance, we calculated the Dice score over the test set. We found that training the framework using all available atlases outperformed ensembling and gave similar results compared to the best of all frameworks trained on a single subject. Furthermore, we found that selecting images from the four atlases closest in gestational age out of all available atlases, regardless of the individual quality, gave the best results with a median Dice score of 0.72. We conclude that our framework can accurately segment and spatially align the embryo in first trimester 3D ultrasound images and is robust for the variation in quality that existed in the available atlases. Our code is publicly available at: https://github.com/wapbastiaansen/multi-atlas-seg-reg.

Keywords: Multi-Atlas Segmentation, Image Registration, Deep Learning, First Trimester Ultrasound, Human Embryo

1. Introduction

The periconception window, which runs from 14 weeks before conception till the end of the first trimester, is crucial for pre- and postnatal health (Steegers-Theunissen et al., 2013). Prenatal growth and development during this period is predominantly monitored via ultrasound imaging (Shengfeng et al., 2019). This is done by manual or semi-automatic measurements of the length and volume of the embryo and detection of standard planes (Salomon et al., 2013). However, these measurements of the embryo are time consuming and prone to human errors (Carneiro et al., 2008). Automating this process would lead to less investigation time and human errors.

Despite its challenges, 3D first trimester ultrasound is suitable for learning based methods, as the whole embryo, thanks to its limited size, can be imaged in one dataset. Here, we propose a deep learning based framework to automatically segment and spatially align the embryo to a standard orientation. These two tasks form the basis for automatic monitoring of growth and development: placing the embryo in an standard orientation enables derivation of the standard planes, and the segmentation of the embryo provides the embryonic volume and simplifies automation of other measurements such as crown-rump length, head circumference and trans-cerebellar diameter (Salomon et al., 2013).

To achieve segmentation and spatial alignment simultaneously, we take an atlas-based registration approach using deep learning. We register all data to an atlas in which the embryo has been segmented and put in a standard orientation. To make our framework applicable to the full first trimester and to increase its robustness to variations in appearance of the embryo across pregnancies, we take a multi-atlas approach by using data of multiple pregnancies with longitudinally acquired images. To address how to combine data from multiple pregnancies we compared three strategies, namely: 1) training the framework using atlas images from a single pregnancy, 2) training the framework with data of all available atlases and 3) ensembling of the frameworks trained per pregnancy. Per ultrasound image, we selected the atlas images closest in gestational age (GA) and we investigated the influence of the number of atlas images that is selected.

By taking an atlas-based registration approach we circumvent the need for ground truth segmentations during training, as atlas-based registration can be fully unsupervised. Manual segmentations of the embryo are laborious to obtain and typically not available, since in clinical practice mainly the length of the embryo and various diameters are used (Salomon et al., 2013). Due to the rapid development of the embryo in the first trimester and wide variation in spatial position and orientation of the embryo and presence of other structures such as placenta, umbilical cord and uterine wall, we choose to add supervision using landmarks to our framework. We proposed to use the crown and rump landmarks of the embryo, since the crown-rump length measurement is relatively easy to obtain and a standard measure in clinical practice (Rousian et al., 2018).

The main contributions of the research presented in this paper are:

- 1. we propose the first automated method to segment and simultaneously spatially align the embryo in 3D ultrasound images acquired during the first trimester;
- 2. we compare different strategies to incorporate data of multiple atlases and address the question how many atlas images to select;

3. we circumvent the need for manual segmentations for training of our framework by relying only on minimal supervision based on two landmarks.

2. Related work

2.1 Segmentation and spatial alignment of prenatal ultrasound

In prenatal ultrasound imaging, most published studies focus on performing spatial alignment and segmentation separately; for a comprehensive overview see Torrents-Barrena et al. (2019). When both spatial alignment and segmentation are of interest performing them sequentially raises the question of the optimal order of operations. Especially since some studies focusing on performing segmentation require prior knowledge about spatial orientation of the embryo (Gutiérrez-Becker et al., 2013; Yaqub et al., 2013) and some studies focusing on standard plane detection require the segmentation or detection of structures within the embryo (Ryou et al., 2016; Yaqub et al., 2015). To circumvent this, a few studies perform both tasks at once (Chen et al., 2012; Kuklisova-Murgasova et al., 2013; Namburete et al., 2018).

Chen et al. (2012) achieved both tasks for the fetal head using spatial features from eye detection and image registration techniques, for ultrasound images acquired at 19-22 weeks GA. However, the eye is not always clearly detectable in 3D first trimester ultrasound, making this method not applicable in our case.

Kuklisova-Murgasova et al. (2013) achieved both tasks for the fetal brain, using a magnetic resonance imaging (MRI) atlas and block matching using image registration techniques, for ultrasound images acquired at 23-28 weeks GA. However, such an atlas or reference MRI image is not available for the first trimester (Oishi et al., 2019).

Namburete et al. (2018) achieved both alignment and segmentation of the fetal head with a supervised multi-task deep learning approach, using slice-wise annotations containing a priori knowledge of the orientation of the head, and manual segmentations, for ultrasound images acquired at 22-30 weeks GA. However, this method assumes that during acquisition the ultrasound probe is positioned such that the head is imaged axially, which is not always the case for 3D first trimester ultrasound.

Although none of the studies are applicable to first trimester ultrasound, they all employ image registration techniques to perform segmentation and spatial alignment simultaneously. In line with this, we take an image registration approach and tailor our method to be applicable to first trimester ultrasound.

2.2 Deep learning for image registration

Recently, deep learning methods for image registration have been developed and show promising results in many areas; for an extensive overview see Boveiri et al. (2020). The common assumption for most of the deep learning approaches for image registration is that the data is already affinely registered. However, due to the rapid development of the embryo and the wide variation in position and spatial orientation the affine registration is challenging to obtain and therefore has to be incorporated in the framework.

There are a few studies focusing on achieving both affine and nonrigid registration. For example, de Vos et al. (2019), proposed a multi-stage framework, dedicating the first network

to learning the affine transformation and the second network to learning the voxelwise displacement field. These networks are trained in stages. Zhengyang et al. (2019) proposed a similar approach where the main difference is that they used a diffeomorphic model for the nonrigid deformation. We also take a multi-stage approach with a dedicated network for the affine and nonrigid deformation. We based the design of both networks on Voxelmorph by Balakrishnan et al. (2019), which is developed for deep learning-based non-rigid image registration and is publicly available.

2.3 Multi-atlas segmentation with deep learning

Using multiple atlases is a common and successful technique for biomedical image segmentation. Adding data of multiple atlases gives in general better and more robust results and is widely used in classical not learning-based methods (Iglesias and Sabuncu, 2015). However, learning-based methods can also benefit from using multiple atlases (Ding et al., 2019; Fang et al., 2019; Lee et al., 2019).

Fang et al. (2019) omits the registration step by directly guiding the training of a segmentation network using multiple atlases as ground truth. Ding et al. (2019) and Lee et al. (2019) both employ deep learning for the image registration step, but they use different strategies for training. Ding et al. (2019) trained a network that warps all available atlas images to the target image at once. On the other hand, Lee et al. (2019) trains the network by giving every epoch a random atlas to the network to register to the target image.

Both approaches train the network to be able to register all available atlases to every image. In our case, the atlases are longitudinally acquired, and due to the rapid development of the embryo, not every atlas matches every image. Hence, we compared different fusion strategies that take this into account.

2.4 Extension of preliminary results

Preliminary results of this framework were published in Bastiaansen et al. (2020a) and Bastiaansen et al. (2020b). In Bastiaansen et al. (2020a) we proposed a fully unsupervised atlas-based registration framework using deep learning for the alignment of the embryonic brain acquired at 9 weeks GA. We showed that having a separate network for the affine and nonrigid deformations improved the results. Subsequently, in Bastiaansen et al. (2020b) our previous work was extended by adding minimal supervision using the crown and rump landmarks to align and segment the embryo.

Here, we substantially extend our previous work by making it applicable to the full first trimester. We achieve this by taking a multi-atlas approach with atlases consisting of longitudinally acquired ultrasound images from multiple pregnancies. We compare different fusion strategies to combine data from multiple pregnancies and address the influence of differences in image quality of the atlas images.

Compared to our previous work, we performed a more in-depth hyperparameter search for our deep learning framework and improved the division of the data in training, validation and test set taking into account the distribution of GA and available information used for evaluation, such as embryonic volume. Finally, to obtain the segmentation of the embryo, in the proposed model the inverse of the nonrigid deformation is needed. To make our

deformations invertible, we adopt a diffeomorphic deformation model as proposed by Dalca et al. (2019), using the stationary velocity field.

3. Method

3.1 Overview

We present a deep learning framework to simultaneously segment and spatially align the embryo in image I. We propose to achieve this by registering every image I to an atlas image via deformation ϕ :

$$A(x) \approx I(\phi(x)) \quad \forall x \in \Omega,$$
 (1)

with Ω the 3D domain of A, I. We assume that the atlas image A is in a predefined standard orientation and the segmentation S_A is available. Now, $I \circ \phi$ is in standard orientation and the segmentation of image I is given by:

$$S_I := S_A \circ \phi^{-1}. \tag{2}$$

The deep learning framework learns to estimate deformation ϕ given at last image A and the image I. We propose to use a multi-at last approach by registering every image to the M at last are closest in GA. In Fig. 1 a detailed overview of our framework can be found; all components are explained in the remainder of this section.

3.1.1 Learning to estimate the deformation ϕ

Firstly, note that our framework consists of two networks, one dedicated to learning an affine transformation and the other to learning a nonrigid deformation. In previous work we showed that separating these tasks was needed due to the wide variety in positions and orientation of the embryo (Bastiaansen et al., 2020a). Therefore, the deformation ϕ consists of an affine transformation ϕ_a and a nonrigid deformation ϕ_d , such that:

$$\phi := \phi_a \circ \phi_d. \tag{3}$$

The affine network to estimate ϕ_a is trained in two stages, the first stage uses the crown and rump landmarks for supervision, while in the second stage the network is trained in an unsupervised way. The nonrigid network to estimate ϕ_d is trained in a fully unsupervised way. ϕ_a and ϕ_d are obtained by two convolutional neural networks (CNN), which model the functions $g_{\theta_{\text{affine}}}$: $(\phi_a, I \circ \phi_a) = g_{\theta_{\text{affine}}}(I)$, with θ_{affine} the network parameters and $g_{\theta_{\text{nonrigid}}}$: $(\phi_d, I_{\phi_a} \circ \phi_d) = g_{\theta_{\text{nonrigid}}}(I_{\phi_a}, A)$, with $I_{\phi_a} = I \circ \phi_a$, and θ_{nonrigid} the network parameters.

3.1.2 The atlas A

To deal with the rapid growth and variation in appearance of the embryo we propose to use a multi-atlas approach. We define $A_{i,j}$ to be an atlas image, with $i=1,...,n_p$, where n_p represents the number of pregnancies and $j \in W$, with W the set of the weeks in which an ultrasound image is available. For example, atlas $A_{1,8}$ represent the atlas image of pregnancy 1 acquired at 8 weeks GA. Define $\mathcal{A} := \{A_{i,j} | i=1,...,n_p, \forall j \in W\}$ to be the set of all available atlases.

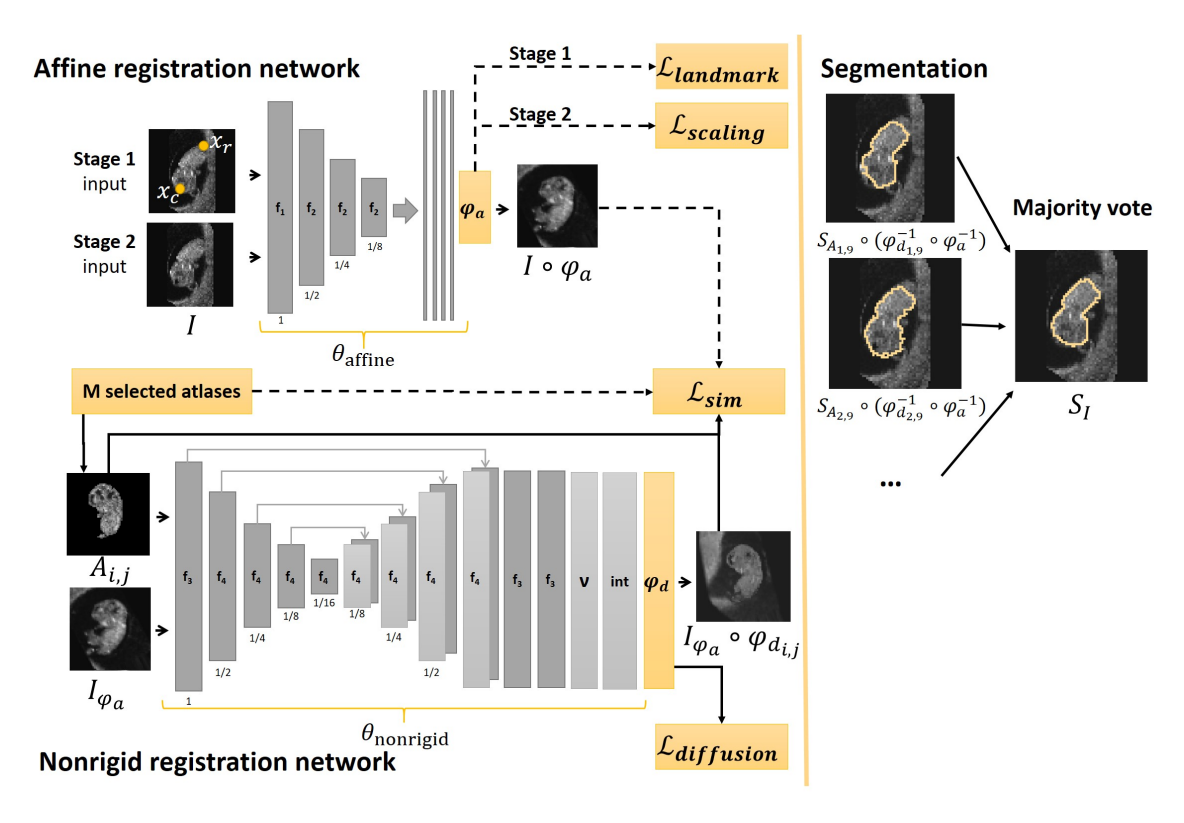


Figure 1: Overview of our framework to register image I to atlas $A_{i,j}$. Atlas $A_{i,j}$ corresponds to pregnancy i with an ultrasound image taken in week j of pregnancy. The network learns the affine and nonrigid deformations ϕ_a and $\phi_{d_{i,j}}$. Using the inverse deformations and majority voting we obtain the segmented images S_I . $I \circ \phi_a$ gives the image I in standard orientation.

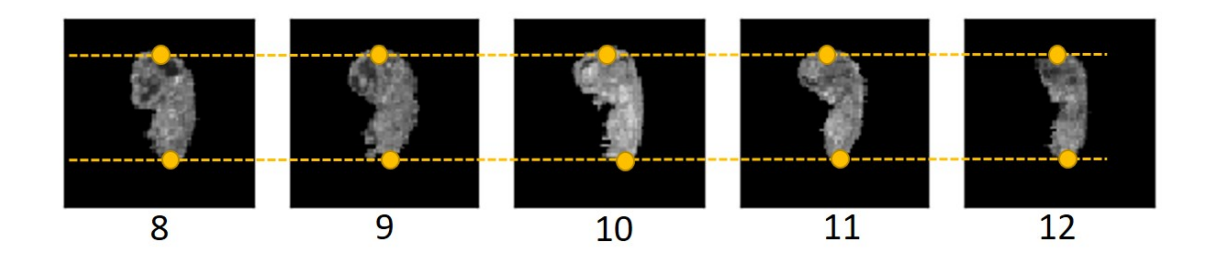


Figure 2: From left to right: example of an atlas at 8, 9, 10, 11 and 12 weeks GA, with their crown and rump landmarks. Actual size of the embryo: 16 mm, 22 mm, 32 mm, 44 mm, 58 mm.

We manually rigidly aligned every atlas $A_{i,j}$ to the same standard orientation. Subsequently, all atlas images, were scaled to the same size by matching the annotated crown and rump landmarks, as shown in Fig. 2. We define the coordinates of the crown and rump landmarks in the standard orientation as $x_c^{\mathcal{A}}$ and $x_r^{\mathcal{A}}$. Finally, the segmentation $S_{A_{i,j}}$ was obtained manually.

3.1.3 Atlas selection and fusion strategies

For every image I the M atlas images closest in GA are selected. Furthermore, from every pregnancy maximally one atlas image is selected, therefore we have: $M \leq n_p$. We define three different atlas fusion strategies:

Single subject strategy The framework is trained using atlas images from a single pregnancy:

$$\mathcal{A}_{k}^{s} := \{ A_{i,j} | i = k, j \in W \} \tag{4}$$

for pregnancy k.

Multi-subject strategy The framework is trained with data of all available atlases:

$$\mathcal{A}^m := \{ A_{i,j} | i = 1, ..., n_p, j \in W \}.$$
 (5)

Ensemble strategy \mathcal{A}^e Ensemble of the results of single subject strategy for $k = 1, ..., n_p$.

3.1.4 Output of framework

The framework outputs the segmentation of the embryo and the embryo in standard orientation. The segmentation S_I is defined as the voxelwise majority vote of:

$$S_I^{i,j} := S_{A_{i,j}} \circ (\phi_{d_{i,j}}^{-1} \circ \phi_a^{-1}).$$
 (6)

over all M selected atlas images. The deformation to put the embryo in standard orientation is given by ϕ_a and the image in standard orientation is given by:

$$I_{\phi_a} := I \circ \phi_a \tag{7}$$

3.2 Affine registration network

The input of the affine registration network is the image I. The affine registration network gives as output the estimated affine transformation ϕ_a and the corresponding affinely registered image $I \circ \phi_a$. Recall that we affinely registered every atlas image to the same standard orientation. Hence, the affine transformation ϕ_a registers the image I to all atlas images in \mathcal{A} . Furthermore, this allowed us to directly compare the image similarity of $I \circ \phi_a$ and all selected atlas images in the loss function. Hence, as shown by the arrows in Fig. 1, in contrast to the nonrigid network, the atlas image $A_{i,j}$ is not given as input to the network.

3.2.1 Network architecture

The affine registration network consists of an encoder, followed by a global average pooling layer. The encoder consist of convolutional layers with a stride of 2, where the images are down-sampled. The numbers of filters (f_1, f_2) are hyperparameters. The global average pooling layer gives as output one feature per feature map, which forces the network to encode position and orientation globally. The pooling layer is followed by four fully connected layers with 1000 neurons and ReLu activation. The output layer consists of the affine transformation ϕ_a and is defined as a 12-dimensional vector containing the coefficients of part of the affine transformation matrix $T \in \mathbb{R}^{4\times 4}$.

3.2.2 Loss function

The loss function for the first training stage of the affine registration network is defined as:

$$\mathcal{L}\left(\mathcal{A}, I, \phi_{a}, x^{\mathcal{A}}, x^{I}\right) = \frac{1}{M} \sum_{i,j} \delta_{i,j} \mathcal{L}_{\text{sim}}\left(A_{i,j}, I \circ \phi_{a}\right) + \lambda_{l} \mathcal{L}_{\text{landmark}}\left(\phi_{a}\left(x^{\mathcal{A}}\right), x^{I}\right),$$

$$(8)$$

with $\delta_{i,j}$ defined as:

$$\delta_{i,j} = \begin{cases} 1 & \text{if } A_{i,j} \text{ selected} \\ 0 & \text{else.} \end{cases}$$
 (9)

The first term of the loss function promotes similarity between the image I after alignment and the atlas. The similarity loss is only calculated within a mask $\tilde{\Omega}$, since there are other objects in the 3D ultrasound images besides the embryo. Mask $\tilde{\Omega}$ is obtained by dilating the union of all segmentations $S_{A_{i,j}} \forall i,j$ using a ball with radius 1. \mathcal{L}_{sim} is chosen as the masked local (squared) normalized cross-correlation (NCC), which is defined as follows:

$$NCC(A,Y) = \frac{1}{|\tilde{\Omega}|} \sum_{p \in \tilde{\Omega}} \frac{\left(\sum_{q} [A(q) - \bar{A}(p)][Y(q) - \bar{Y}(p)]\right)^{2}}{\left(\sum_{q} [A(q) - \bar{A}(p)]^{2}\right) \left(\sum_{q} [Y(q) - \bar{Y}(p)]^{2}\right)},$$
(10)

where \bar{A} (and similarity for \bar{Y}) denote: $\bar{A}(p) = A(p) - \frac{1}{j^3} \sum_q A(q)$, where q iterates over a j^3 volume around $p \in \Omega$ with j = 9 as in Balakrishnan et al. (2019). The second term in Eq. 8 minimizes the mean squared error in voxels between the landmarks after registration and is defined as:

$$\mathcal{L}_{landmark}\left(\phi_{a}\left(x^{\mathcal{A}}\right), x^{I}\right) = \frac{1}{n_{l}} \sum_{i=1}^{n_{l}} \left(x_{i}^{I} - \phi_{a}\left(x_{i}^{\mathcal{A}}\right)\right)^{2}, \tag{11}$$

with n_l the number of annotated landmarks, with $n_l = 2$ in our case.

During the second stage of training the weights θ_{affine} learned in the first stage are used as initialization of the network. The loss function for the second training stage of the affine registration network is defined as:

$$\mathcal{L}(\mathcal{A}, I, \phi_a) = \frac{1}{M} \sum_{i,j} \delta_{i,j} \mathcal{L}_{\text{sim}} (A_{i,j}, I \circ \phi_a)$$

$$+ \lambda_s \mathcal{L}_{\text{scaling}} (\phi_a),$$
(12)

where $\mathcal{L}_{\text{sim}} = -\text{NCC}(A_{i,j}, I \circ \phi_a)$ as defined in Eq. (10). When objects in the background are present, penalizing extreme zooming is beneficial, as was showed in Bastiaansen et al. (2020a). Hence, $\mathcal{L}_{\text{scaling}}$ is defined as:

$$\mathcal{L}_{\text{scaling}}(\phi_a) = \sum_{i=1}^{3} \log(s_i)^2, \tag{13}$$

following Ashburner et al. (1999), with s_i the scaling factors of ϕ_a obtained using the singular value decomposition.

3.3 Nonrigid registration network

The input of the nonrigid registration network is an affinely registered image $I_{\phi_a} := I \circ \phi_a$ together with a selected atlas image $A_{i,j}$. During training we provide as input to the network the image I and one randomly chosen selected atlas image $A_{i,j}$. During inference we give as input to the network all the possible pairs of image and selected atlas image. The output of the network consists of $\phi_{d_{i,j}}$, along with the registered images $I_{\phi_a} \circ \phi_{d_{i,j}}$.

To obtain the segmentation in Eq. 6, the deformation $\phi_{d_{i,j}}$ must be inverted. To ensure invertibility, we adopt diffeomorphic deformation for $\phi_{d_{i,j}}$. Following Dalca et al. (2019), we use a stationary velocity field (SVF) representation, meaning that $\phi_{d_{i,j}}$ is obtained by integrating the velocity field ν (Ashburner, 2007). Now, $\phi_{d_i}^{-1}$ is obtained by integrating the velocity field using $-\nu$.

3.3.1 Network architecture

For the nonrigid registration network we used the architecture of Voxelmorph proposed by Balakrishnan et al. (2019). Voxelmorph consists of an encoder, with convolutional layers with a stride of 2, a decoder with convolutional layers with a stride of 1, skip-connections, and an up-sampling layer. This is followed by convolutional layers at full resolution, to refine the velocity field ν . The numbers of filters (f_3, f_4) are hyperparameters. The velocity field ν is integrated in the integration layer to give the dense displacement field. In both networks, all convolutional layers have a kernel size of 3 and have a LeakyReLU activation with parameter 0.2.

3.3.2 Loss function

The loss function for the nonrigid registration network is:

$$\mathcal{L}(A_{i,j}, I_{\phi_a}, \phi_{d_{i,j}}) = \mathcal{L}_{\text{sim}} \left(A, I_{\phi_a} \circ \phi_{d_{i,j}} \right) + \lambda_{\text{d}} \mathcal{L}_{\text{diffusion}} \left(\phi_{d_{i,j}} \right), \tag{14}$$

where $I_{\phi_a(x)} := I \circ \phi_a$ is the output of the affine network. \mathcal{L}_{sim} is again defined as the NCC in Eq. 10. $\phi_{d_{i,j}}$ is regularized by:

$$\mathcal{L}_{\text{diffusion}}\left(\phi_{d_{i,j}}\right) = \frac{1}{|\tilde{\Omega}|} \sum_{p \in \tilde{\Omega}} \|\nabla d_{i,j}(p)\|^2, \tag{15}$$

This loss term penalizes local spatial variations in $\phi_{d_{i,j}}$ to promote smooth local deformations (Balakrishnan et al., 2019).

3.4 Implementation details

For training the ADAM optimizer was used with a learning rate of 10^{-4} , as in Balakrishnan et al. (2019). For the second training stage of the affine registration network, we lower the learning rate to 10^{-5} , since the network has already largely converged in the first stage. We trained each part of the network for 300 epochs with a batch size of one. In the first training stage of the affine network data augmentation was applied. Each scan in the training set was either randomly flipped along one of the axes or rotated 90, 180 or 270 degrees. For the second stage and nonrigid network preliminary experiments showed that data augmentation did not improve the results. The framework is implemented using Keras (Chollet and et al., 2015) with Tensorflow as backend (Abadi et al., 2016). The code is publicly available at: https://github.com/wapbastiaansen/multi-atlas-seg-reg

4. Experiments

4.1 The Rotterdam Periconceptial Cohort

The Rotterdam Periconceptional Cohort (Predict study) is a large hospital-based cohort study conducted at the Erasmus MC, University Medical Center Rotterdam, the Netherlands. This prospective cohort focuses on the relationships between periconceptional maternal and paternal health and embryonic and fetal growth and development (Rousian et al., 2021; Steegers-Theunissen et al., 2016). 3D ultrasound scans are acquired at multiple points in time during the first trimester. Ultrasound examinations were performed on a Voluson E8 or E10 (GE Healthcare, Austria) ultrasound machine. Furthermore, maternal and paternal food questionnaires are taken and other relevant data such as weight, height and bloodsamples are collected.

4.1.1 In- and exclusion criteria

Women are eligible to participate in the Rotterdam Periconception Cohort if they were at least 18 years of age, with an ongoing singleton pregnancy less then 10 weeks of GA. Pregnancies were only included if the GA could be determined reliably and the pregnancy did not end in miscarriage, discontinuation, intra-uterine fetal death, stillbirth, or passing away postpartum. GA was calculated according to the first day of the last menstrual period (LMP), and in cases with an irregular menstrual cycle, unknown LMP or a discrepancy of more then seven days, GA was determined by the crown-rump length measurements performed in the first trimester. In case of conception by means of in vitro fertilisation or intracytoplasmic sperm injection, the conception date was used to calculate the GA. We included pregnancies regardless of the mode of conception.

We included images that had sufficient quality to manually annotate the crown and rump landmarks. We included pregnancies with ultrasound images acquired between 8+0 and 12+6 weeks GA. This range was selected, since previous research by Rousian et al. (2013) showed that firstly the crown and rump landmarks could be reliably determined up until and including the 12th week of pregnancy, and secondly that other relevant measurements which are relevant for more in-depth insight in growth and development, such as head circumference, trans-cerebellar diameter, biparietal diameter and abdominal circumference can be measured reliable starting at a GA of 7+4.

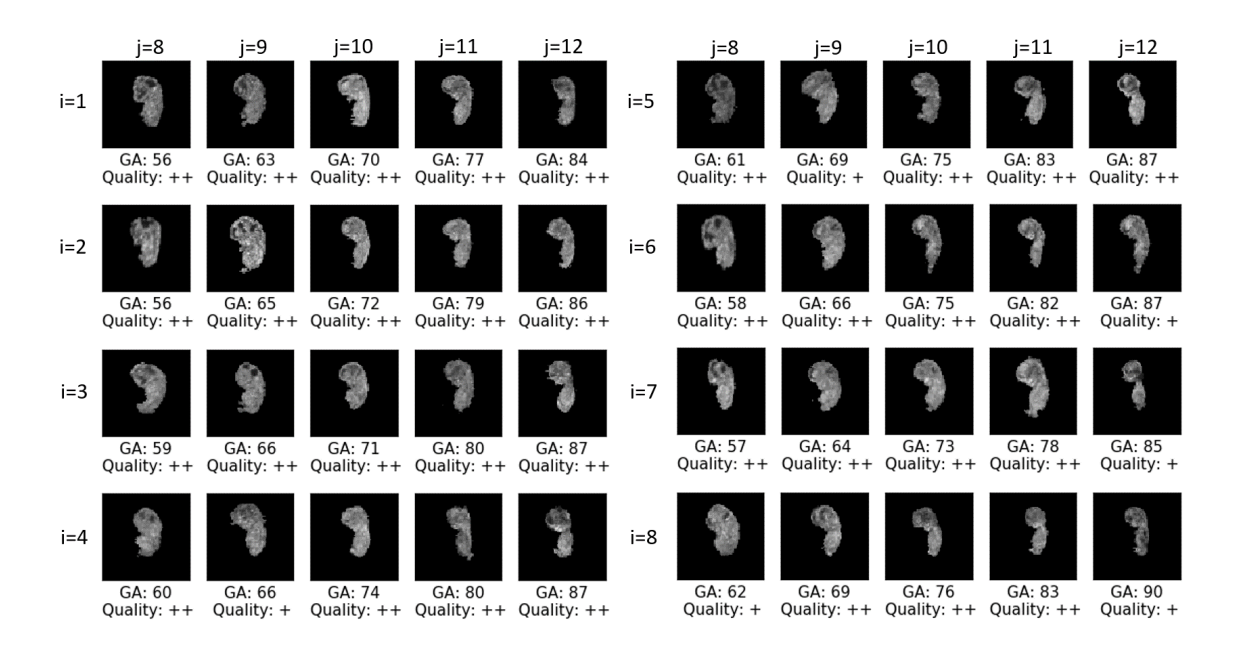


Figure 3: Overview of all atlases $A_{i,j}$ with i = 1, ..., 8 the number of the pregnancy and J = 8, 9, 10, 11, 12 the week of pregnancy the ultrasound image was made. Below the gestational age (GA) is given along with the image quality score giving during EV measurements in Virtual Reality. ++: good quality, +: sufficient quality, -: poor quality.

4.1.2 Manual annotations and image pre-processing

In the Predict study the embryonic volume (EV) is semi-automatically measured using Virtual Reality techniques (Rousian et al., 2018). We choose to use the available EV measurements for evaluation and refer to them as EV_{gt} . Additionally, for 186 images corresponding segmentations were saved. We used these segmentation, referred to as S_I^{gt} , for evaluation as well.

The included images have isotropic voxel sizes varying between 0.06 mm and 0.75 mm. The resolution varied between 121 and 328 voxels in the first dimension, between 83 and 257 voxels in the second dimension and 109 and 307 voxels in the third dimension. To speed up training all images were re-scaled to $64 \times 64 \times 64$ voxels. To achieve this while keeping isotropic voxel sizing, all images were padded with zeros to a square shape and subsequently rescaled to the right size.

4.1.3 Atlas, training, validation and test set

We included data of 1282 pregnancies collected between December 2009 and August 2018. Eight pregnancies were used to create the atlas images, the remaining 1274 pregnancies were divided as follows over the training set (874, 68%), independent test set (200, 16%) and validation set (200, 16%) for hyperparameter optimization and fusion strategy comparison.

The eight pregnancies that formed the atlas images were selected because they had weekly ultrasound images and had the highest overall image quality rating, this rating was assigned during the measurement in Virtual Reality (Rousian et al., 2013). We choose to

use eight atlases since adding more did not lead to improved performance in preliminary experiments. The choice to consider only pregnancies with weekly images was made to ensure that we would have a good representation of every week GA among the atlases. In Fig. 3 a visualization of all atlases along with their GA in days and quality score can be found. We divided pregnancies over the train, validation and test set by following the rules below in the given order:

- 1. all segmentations S_I^{gt} must be divided equally over the validation and test set;
- 2. all data of a pregnancy should be in the same set;
- 3. the majority of the EV measurements should correspond to images in the validation or test set.
- 4. within every week GA the division of unique pregnancies is approximately 60 % 20% 20% over train, validation and test set.

In Tab. 1 the characteristics of the final split can be found.

4.2 Evaluation metrics

The following two metrics were used to evaluate the results. Firstly, we report the relative error between the volume calculated from estimated segmentation S_I , referred to as EV(I), and the ground truth embryonic volume $EV_{gt}(I)$:

$$EV_{error}(I) := \frac{|EV(I) - EV_{gt}(I)|}{EV_{gt}(I)}.$$
(16)

Secondly, we report the Dice similarity coefficient between the available manual segmentations $S_I^{\rm gt}$ and the estimated segmentation S_I of the image I (Dice and Lee, 1945). To compare the results of different experiments, we performed the two-sided Wilcoxon signed-rank test with a significance level of 0.05, we report the p-values for both metrics as p_{EV} and p_{Dice} .

Table 1: Characteristics of the splitting of the data. Per gestational week the number of unique pregnancies, images, images with embryonic volume measurement (EV) and images with a ground truth segmentation (seg) is given.

	Training			Validation			Test					
week	preg	img	EV	seg	preg	img	EV	seg	preg	img	EV	seg
8	252	457	373		64	142	130		63	156	130	
9	605	1333	1112		195	404	394	34	193	396	394	34
10	237	551	376		81	150	140		83	156	150	
11	463	1190	865		193	420	387	58	194	428	408	60
12	185	407	193		68	122	121		67	113	113	
all	874	3938	2919		200	1238	1172	92	200	1249	1205	94

4.3 Experiments

We performed the following six experiments.

Experiment 1: sensitivity metrics

In literature there are no comparable studies available, to get insight in the performance of the presented framework we addressed the sensitivity to perturbations of the used evaluation metrics. We performed four operations on the 186 available ground truth segmentations: dilation using a ball with radius of one voxel; erosion using a ball with a radius of one voxel; dilation using a ball with a radius of two voxels; erosion using a ball with a radius of two voxels. We compared the four obtained segmentations with the original segmentation and report the mean and standard deviation of every operation.

Experiment 2: influence of hyperparameters

Using the single subject strategy \mathcal{A}_1^s we performed a hyperparameter search on the validation set for $\lambda_l \in \{0.01, 1, 100\}$ in Eq. 8, $\lambda_s \in \{0, 0.005, 0.05, 0.5, 5\}$ in Eq. 12 and $\lambda_d \in \{1, 10, 100\}$ in Eq. 14 and the number of filters (f_1, f_2) with $f_2 = 2f_1$ and $f_1 \in \{16, 32, 64\}$ in the encoder of the affine network and (f_3, f_4) with $f_4 = 2f_3$ and $f_3 \in \{1, 2, 4, 8, 16\}$ in the encoder and decoder of the nonrigid network. Furthermore, we took out training stage 2 of the affine network to evaluate its necessity, we call this strategy \mathcal{A}_1^{s*} .

Experiment 3: single subject strategy

We used the best hyperparameters from experiment 2 to train \mathcal{A}_k^s for k=2,3,...,8 and compare the results on the validation set to the results for \mathcal{A}_1^s , to evaluate whether the choice of pregnancy k influences the results. Finally, we applied \mathcal{A}_k^s for best performing pregnancy k to the test set.

Experiment 4: comparison of the multi-subject and ensemble strategy

To evaluate what is the best approach to combine data of multiple pregnancies we compared the results on the validation set of the multi-subject strategy \mathcal{A}^m for $M=1,\,M=2,\,M=4$ and M=8 to the ensemble strategy \mathcal{A}^e .

Experiment 5: influence of atlas image quality

We investigated the influence of the quality of the ultrasound images on the results by excluding pregnancy i = 8, since this pregnancy had the lowest quality score (see Fig. 3). We repeated experiment 4 without pregnancy i = 8 on the validation set and compared the results to the original results in experiment 4.

Experiment 6: Analysis of the best models

We compared the best strategy using data of multiple pregnancies to the best single subject strategy on the test set to investigate whether utilizing data of multiple pregnancies improves the results. For the best performing model, we analyzed the results per week GA and visualized the resulting segmentations S_I and aligned images $I \circ \phi_a$. Finally, to gain more insight into reasons why our framework might fail we visually inspected all images in the test set having a EV_{error} higher than Q_3 .

Table 2: Mean EV_{error} and Dice score for the four operations. Standard deviation is given between brackets. The radius of the ball is given in voxels.

	(a) EV_{erro}	r	(b) Dice			
Radius	Dilation	Erosion	Radius	Dilation	Erosion	
1	0.37 (0.06)	0.31 (0.05)	1	0.84 (0.02)	0.81 (0.03)	
2	0.83 (0.17)	0.55 (0.07)	2	0.71 (0.04)	0.61 (0.07)	

5. Results

5.1 Experiment 1: sensitivity metrics

We performed four operations on the 186 available ground truth segmentations to investigate the sensitively to pertubations, in Tab. 2 the mean EV_{error} and Dice score can be found.

5.2 Experiment 2: influence of hyperparameters

In Fig. 4 the mean EV_{error} and mean Dice score can be found for the validation set for different hyperparameters. For the first stage of the affine registration network, the best results were found for $\lambda_l = 1$ and $(f_1, f_2) = (32, 64)$. Setting $\lambda_l = 0.01$ gave worse results since then in the optimization the supervison by landmarks is neglected. For $\lambda_l = 100$ the results are worse, since in this case the image similarity term in Eq. (8) is neglected in the optimization.

Furthermore, Fig. 4 shows that after applying the second training stage of the affine network in general the results improved. Only for $\lambda_s = 5$ the results deteriorate, which is caused by penalizing scaling too much. The best results were found for $\lambda = 0.05$.

Regarding the results of training the nonrigid registration network, Fig. 4 shows that setting $\lambda_d = 100$ results in low flexibility of the deformation field, which leads to no improvements of the results after nonrigid registration. Setting $\lambda_d = 1$ resulted in irregular deformation fields. The best results were found for $\lambda_d = 10$ and $(f_3, f_4) = (8, 16)$.

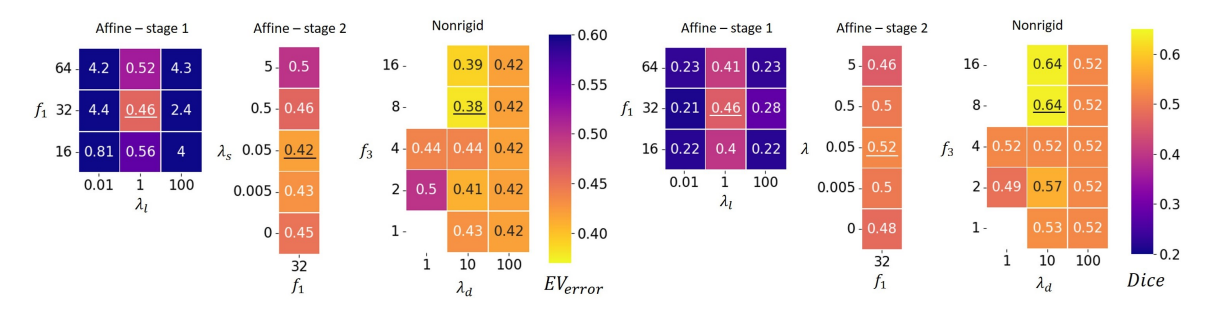


Figure 4: The mean Error_{EV} and mean Dice score over the validation set for different values of λ_l in (8), λ_s in (12), λ_d in (14) and the number of filters $(f_1, 2f_1)$ in the affine network and $(f_3, 2f_3)$ in the nonrigid network. Result for the best combination of hyperparameters is underlined. Hyperparameter combinations that did not converge are blank.

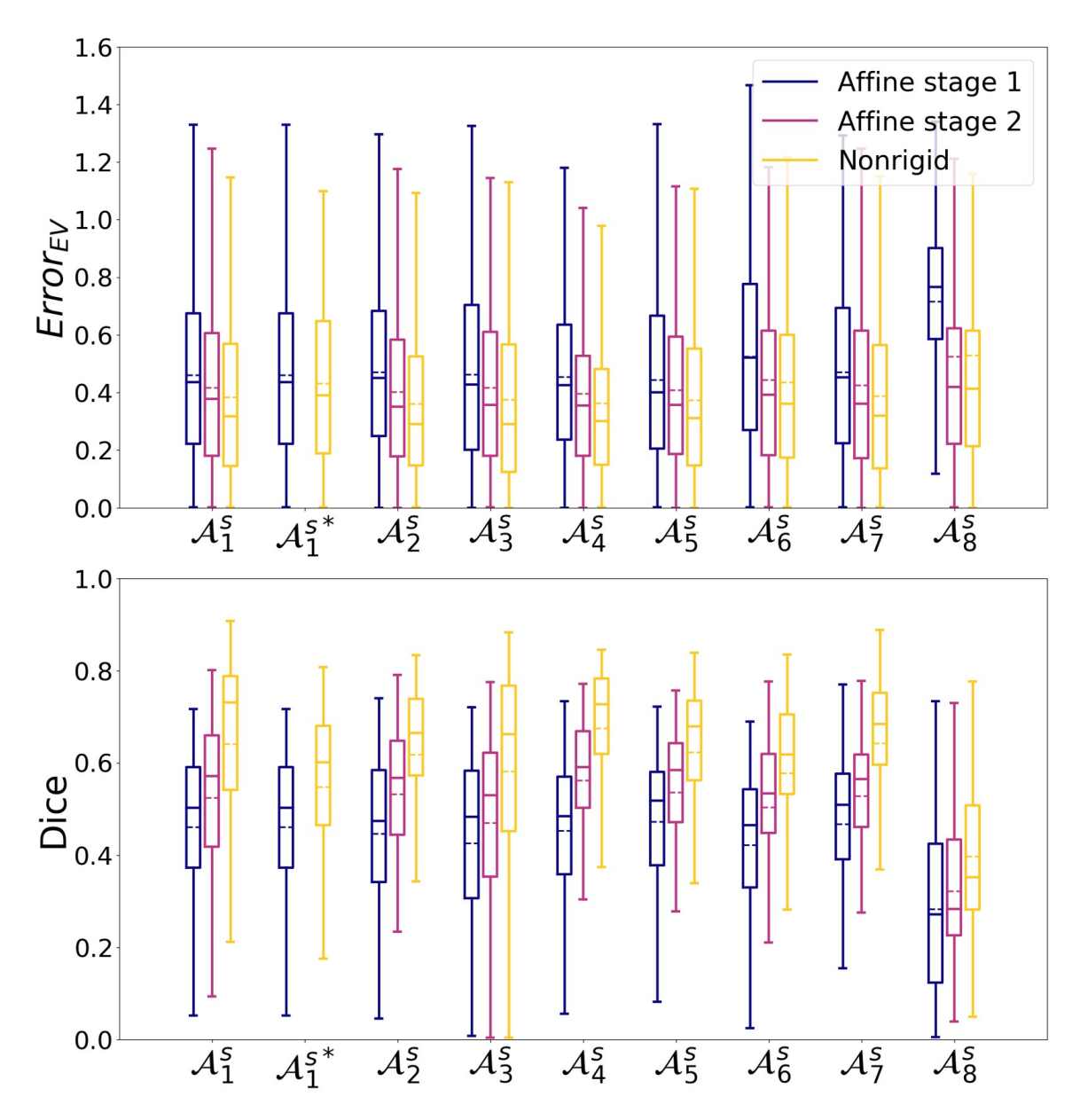


Figure 5: Results for all eight single subject strategies evaluated over the validation set. \mathcal{A}_1^{s*} refers to the single subject strategy where stage 2 of the affine network is omitted. The dotted line represents the mean.

Finally, we compared using the results of stage 2 (\mathcal{A}_1^s) or the results of stage 1 (\mathcal{A}_1^{s*}) as input for the nonrigid registration network. Comparing the results for \mathcal{A}_1^s and \mathcal{A}_1^{s*} in Fig. 5 shows that the results are better for both metrics for \mathcal{A}_1^s . The statistical test confirmed these observations ($p_{EV} < 0.001$, $p_{Dice} < 0.01$).

5.3 Experiment 3: single subject strategy

Using the best hyperparameters determined in experiment 2, we trained the framework using the single subject strategy for every pregnancy k = 1, ..., 8. Fig. 5 shows for the validation set that for \mathcal{A}_k^s , for k = 1, ..., 8 the results improved between the stages of the affine network and after nonrigid registration. Furthermore, a wide spread is observed in the results, which comes from cases where the affine registration fails and this can not be compensated for by the subsequent nonrigid registration network. In general our approach gives similar results independent of the choice of atlas. However, there are differences in results between the different pregnancies, that are consistent with the variation in atlas image quality.

We applied the framework on the test set using the best hyperparameters found and the best single subject strategy. Fig. 5 shows that \mathcal{A}_4^s performs the best in terms of Dice score and comparable in terms of EV_{error}. Fig. 6 shows that the results on the test set are comparable to those on the validation set for \mathcal{A}_4^s .

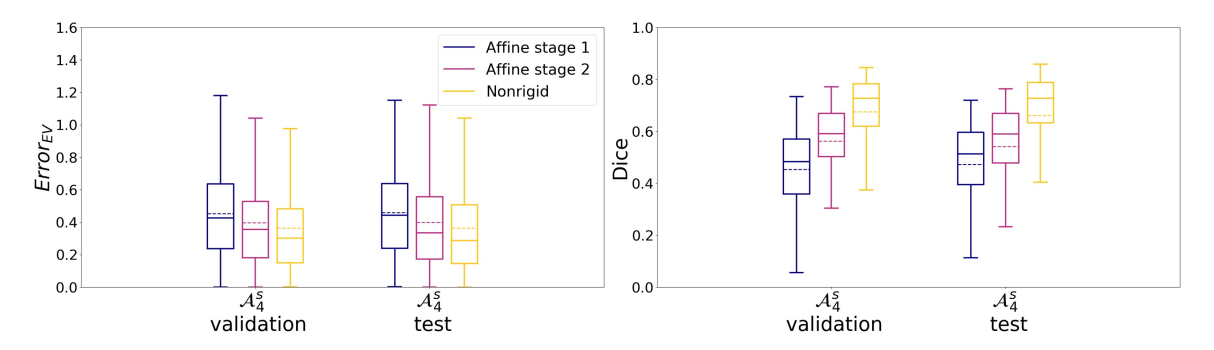


Figure 6: Boxplots of results for single subject strategy \mathcal{A}_4^s for the validation and test set. The dotted line represents the mean.

Table 3: P-values of the two-side Wilcoxon signed-rank test for both metrics over the validation set. Statistically significant results are boldface.

$EV_{ m error}$	$\mathcal{A}^m, M = 1$	$\mathcal{A}^m, M=2$	$\mathcal{A}^m, M=4$	$\mathcal{A}^m, M=8$	\mathcal{A}^e
$\mathcal{A}^m, M=1$		< 0.001	< 0.001	0.064	< 0.001
$\mathcal{A}^m, M=2$	0.001		0.780	0.005	< 0.001
$\mathcal{A}^m, M=4$	< 0.001	0.016		0.051	< 0.001
$\mathcal{A}^m, M = 8$	< 0.001	0.147	0.304		< 0.001
\mathcal{A}^e	< 0.001	0.006	0.471	0.052	

5.4 Experiment 4: comparison of the multi-subject and ensemble strategy

In experiment 4 we compared the multi-subject strategy \mathcal{A}^m , for different values of M, with the ensemble strategy \mathcal{A}^e . Fig. 7a show that using the multi-subject strategy \mathcal{A}^m gives for all tested values of M better results than taking the ensemble strategy \mathcal{A}^e . This is confirmed by the statistical test for the EV_{error} (see Tab. 3). Overall, the results for \mathcal{A}^m with M=4 are the best with a median EV_{error} = 0.32 and median Dice Score = 0.72.

5.5 Experiment 5: influence of quality atlas images

After excluding pregnancy i=8 with the lowest image quality, experiment 4 was repeated. Fig. 7b shows that for multi-pregnancy strategy \mathcal{A}^m with M=1 and the ensemble strategy \mathcal{A}^e the results are significantly better when excluding the pregnancy with lowest image quality (\mathcal{A}^m , M=1: $p_{EV}=0.001$, $p_{Dice}<0.001$, $p_{Dice}<0.001$, $p_{Dice}<0.001$). This can be explained by the fact that if fewer atlases are taken into account, atlas images with worse quality will have more influence. When comparing the multi-pregnancy strategy \mathcal{A}^m with M=7 against the multi-pregnancy strategy \mathcal{A}^m with M=8 only the EV_{error} was significantly better for M=7 ($p_{EV}=0.01$, $p_{Dice}=0.43$). For the multi-pregnancy strategy with M=2 and M=4 the results were not significantly different (M=2: $p_{EV}=0.22$, $p_{Dice}=0.12$, M=4: $p_{EV}=0.40$, $p_{Dice}=0.45$).

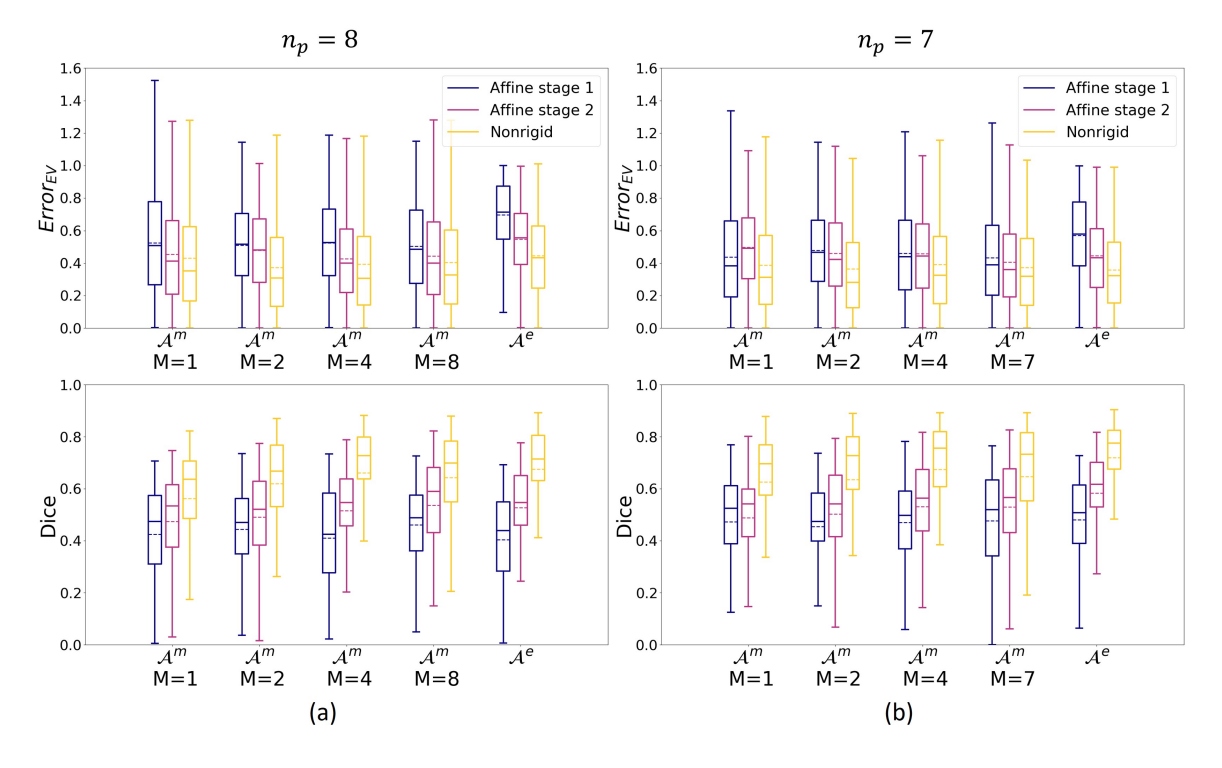


Figure 7: (a) Results for the validation set for experiment 4, where multi-subject strategy \mathcal{A}_m for different values of M is compared to the ensemble strategy \mathcal{A}^e . (b) Results for the validation set for experiment 5, where experiment 4 is repeated without the data of pregnancy i = 8 with the lowest image quality.

5.6 Experiment 6: Analysis of the best models

The results for the best single subject strategy \mathcal{A}_4^s and best multi-subject strategy \mathcal{A}^m with M=4 were compared on the test set and no significant differences were found ($p_{EV}=0.75$, $p_{Dice}=0.71$). Taking the multi-subject strategy with M=4 omits choosing the right pregnancy as atlas and in experiment 5 we saw that the results are not affected by the presence of atlas images with lower image quality. Therefore, we conclude that the multi-subject strategy with M=4 is a robust method.

Next, multi-subject strategy \mathcal{A}^m with M=4 was analyzed in more detail. Fig. 8a shows that distribution of the estimate EV and the ground truth EV_{gt} per week GA is similar. This indicates that our method is robust for the variation due to rapid growth and development over time. Fig. 8b shows for every gestational week the mid sagittal plane of an image from the test set. GA, EV_{error} and Dice score are given per image.

Finally, we visually inspected all images in the test set with a EV_{error} above Q_3 . We observed that for 8% of the images the embryo was lying against the border of the image, for 47% of the images the embryo was lying against the uterine wall, for 34% the image quality was very low due to noise, low contrast or motion artefacts and for 11% of the images there was no apparent visual cue why the affine registration might fail. Fig. 9 shows some examples of an embryo lying against the border of the image, of the embryo lying against the uterine wall and of low image quality.

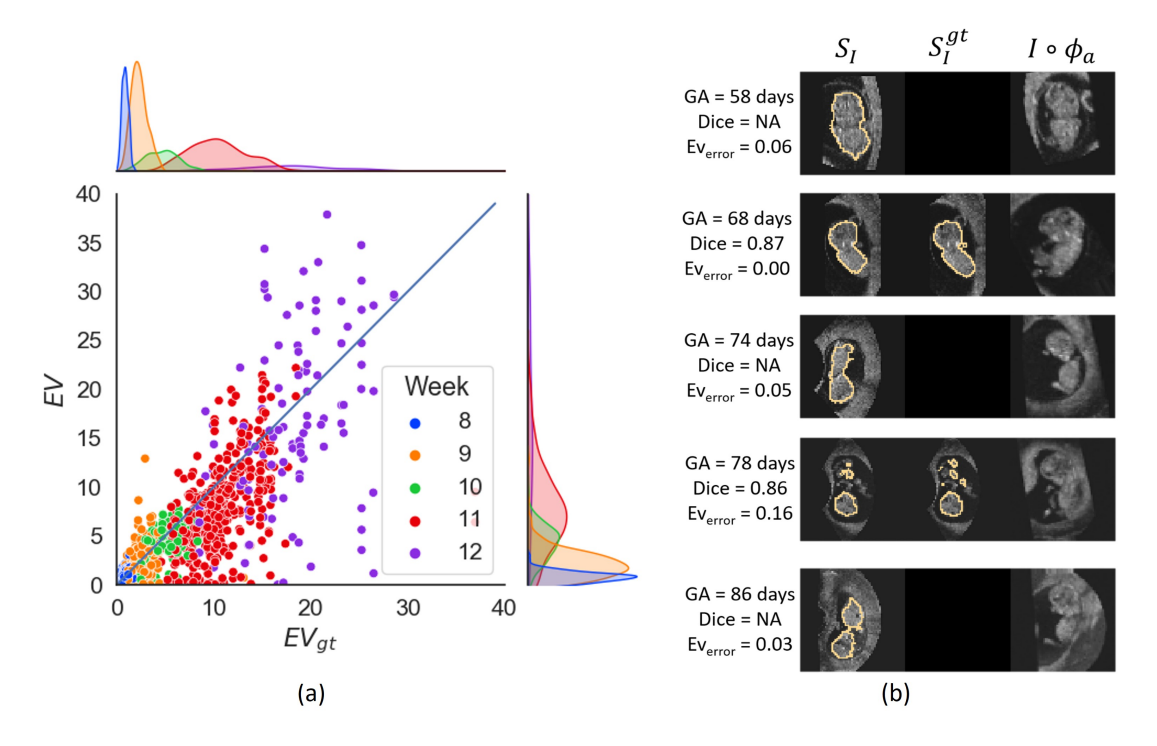


Figure 8: Results of multi-pregnancy strategy \mathcal{A}^m with M=4 for the test set. (a) joint plot for EV and EV_{gt} in mm³, per gestational week. (b) For every week GA the midsaggital plane of an image from the test set is shown. The slice shown for S_I corresponds to the slice of the midsaggital plane in the standard orientation.

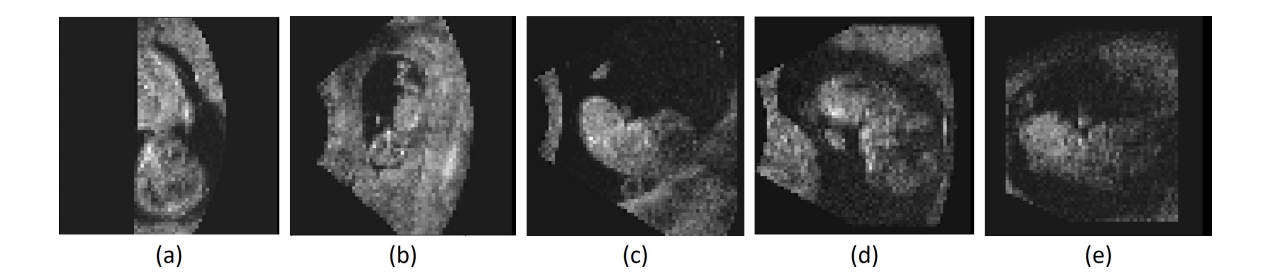


Figure 9: Examples of the original image for which the affine registration network failed. (a) example of an image where the embryo lies in the image border. (b,c) examples of images where the embryo lies against the uterine wall and there is no clear distinction between embryo and uterine wall. (d,e) examples of images with low quality.

6. Discussion and conclusion

Monitoring first trimester embryonic growth and development using ultrasound is of crucial importance for the current and future health of the fetus. A first key step in automating this monitoring, is achieving automatic segmentation and spatial alignment of the embryo. Automation of those tasks will result in less investigation time and human errors. Here we present the first framework to perform both tasks simultaneously for first trimester 3D ultrasound images. We have developed an multi-atlas segmentation framework and showed we could accurately segment and spatially align the embryo captured between 8+0 and 12+6 weeks GA.

We evaluated three atlas fusion strategies for deep learning based multi-atlas segmentation, namely: 1) single-subject strategy: training the framework using atlas images from a single pregnancy, 2) multi-subject strategy: training the framework with data of all available atlas images and 3) ensemble strategy: ensembling of the frameworks trained per pregnancy. The results on the test set for the best single subject strategy were a median relative embryonic volume error of 0.29 and median Dice score of 0.73. The multi-subject strategy significantly outperformed the ensembling strategy and the best results on the test set were found when taking the M=4 atlas images closest in gestational age in account (median $\mathrm{EV}_{\mathrm{error}}=0.32$, median $\mathrm{Dice}=0.72$). The best single subject strategy and the best multi-subject strategy did not significantly outperform each other. However, the multi-subject strategy circumvents the need for selecting the most suitable pregnancy to create atlas images and is therefore a more robust method.

Regarding the values of the metrics for taking a multi-subject approach with M=4, we observed that dilation and erosion of the ground truth segmentations with a ball with a radius of one voxel gave a mean Dice score of 0.84 and 0.81 and a mean EV_{error} of 0.37 and 0.31. The results found in the experiments were for the embryonic volume error in the same range.

We took a deep learning approach for image registration. Our framework consist of two networks, the first one dedicated to learning the affine transformation and the second one to learning a nonrigid registration. The affine network is trained in two stages: the first stage is trained supervised using the crown and rump landmarks and subsequently in the second stage the results is refined in an unsupervised manner. In our experiments using

the single subject strategy we showed that this second stage significantly improves the final result over skipping this stage. The nonrigid network is trained fully unsupervised. We performed an rigorous search to select the hyperparameters. Training the framework for all eight single subject strategies gave on the validation set similar results for the selected hyperparameters.

The multi-subject strategy outperfored the ensemble strategy. The key difference between these two techniques is the way they were trained. In the multi-subject strategy one network was trained using all available atlases. In the ensemble strategy eight individual networks were trained. We saw that, when excluding the pregnancy that gave the worst individual results, this ensemble significantly outperformed the original one. Hence, in this set-up taking an ensembling approach is influenced by the individual results. Taking the multi-subject strategy is a robust approach against this, since during training all atlas images were presented.

For the multi-subject strategy we evaluated how many images M should be registered to every image I. A possible explanation why M < 4 was not optimal is that this may not present enough variation to find a suitable match for every image I. Taking M > 4, leads to a comparison with atlases covering a wide age range. This happens because the atlas images cover almost every day with 8+0 and 12+6 weeks gestation, see Fig. 3. This wide age range might result in some atlases not matching with the image, due to the rapid development of the embryo.

The main limitation of our work is that when the affine registration fails, the nonrigid network cannot correct for this. This resulted in a wide spread in the results that was propagated from the affine to the nonrigid network for both metrics and all atlas fusion strategies. We observed that cases with a high relative embryonic volume error (EV_{error} > Q_3) had clear visual explanation for the failing of the registration: either the embryo lying on the image border, against the uterine wall or the image had low quality. A good direction for further research might be to use the embryonic volume error during training. Having the embryonic volume available during training might simplify finding the embryo.

Finally, another interesting topic for further research is applying our framework to other problems. We created a flexible framework that easily can be adapted to work with or without landmarks and with or without multiple atlas images. Furthermore, these atlas images could be longitudinal, like presented here, but the framework can also be applied to cross-sectional atlas images. The atlas selection is currently based on gestational age, but could be based on any other relevant meta-data.

We conclude that the presented multi-atlas segmentation and alignment framework enables the first key steps towards automatic analysis of first trimester 3D ultrasound. Automated segmentation and spatial alignment pave the way for automated biometry and volumetry, standard plane detection, abnormality detection and spatio-temporal modelling of growth and development. This will allow for more accurate and less time-consuming early monitoring of growth and development in this crucial period of life.

Acknowledgments

The authors thank the Rotterdam Periconception Cohort team of the department of Obstetrics and Gynaecology for data acquisition and the participating couples and researchers for their contributions. This research was funded by the Erasmus MC Medical Research Advisor Committee (grant number: FB 379283).

Ethical Standards

This study was approved by the local Medical Ethical and Institutional Review Board of the Erasmus MC, University Medical Center, Rotterdam, The Netherlands. Prior to participation, all participants provided written informed consent.

Conflicts of Interest

Wiro Niessen is founder, shareholder and scientific lead of Quantib BV. The authors declare no other conflicts of interest.

References

- M. Abadi, A. Agarwal, P. Barham, E. Brevdo, Z. Chen, C. Citro, G. S. Corrado, A. Davis, J. Dean, M. Devin, S. Ghemawat, I. Goodfellow, A. Harp, G. Irving, M. Isard, Y. Jia, R. Jozefowicz, L. Kaiser, M. Kudlur, J. Levenberg, D. Mane, R. Monga, S. Moore, D. Murray, C. Olah, M. Schuster, J. Shlens, B. Steiner, I. Sutskever, K. Talwar, P. Tucker, V. Vanhoucke, V. Vasudevan, F. Viegas, O. Vinyals, P. Warden, M. Wattenberg, M. Wicke, Y. Yu, and X. Zheng. TensorFlow: Large-Scale Machine Learning on Heterogeneous Distributed Systems. 2016. URL http://arxiv.org/abs/1603.04467.
- J. Ashburner. A fast diffeomorphic image registration algorithm. *NeuroImage*, 38:95–113, 2007.
- J. Ashburner, J. L.R. Andersson, and K. J. Fristen. Image registration using a symmetric prior- in three-dimensions. *NeuroImage*, 9:212–225, 1999.
- G. Balakrishnan, A. Zhao, M. R. Sabuncu, J. Guttag, and A. V. Dalca. Voxelmorph: a learning framework for deformable medical image registration. *IEEE TMI*, 38:1788–1800, 2019.
- W.A.P. Bastiaansen, M. Rousian, R.P.M. Steegers-Theunissen, W.J. Niessen, A. Koning, and S. Klein. Towards segmentation and spatial alignment of the human embryonic brain using deep learning for atlas-based registration. In *Biomedical Image Registration*, pages 34–43, 2020a.
- W.A.P. Bastiaansen, M. Rousian, R.P.M. Steegers-Theunissen, W.J. Niessen, Anton Koning, and Stefan Klein. Atlas-based segmentation of the human embryo using deep learning

- with minimal supervision. In Medical Ultrasound, and Preterm, Perinatal and Paediatric Image Analysis, pages 211–221. Springer, 2020b.
- H.R. Boveiri, R. Khayami, R. Javidan, and A. Mehdizadeh. Medical image registration using deep neural networks: A comprehensive review. Computers & Electrical Engineering, 87: 106767, 2020.
- G. Carneiro, B. Georgescu, S. Good, and D. Comaniciu. Detection and measurement of fetal anatomies from ultrasound images using a constrained probabilistic boosting tree. *IEEE Trans Med Imaging*, 27(9):1342–1355, 2008.
- H. C. Chen, P. Y. Tsai, H. H. Huang, H. H. Shih, Y. Y. Wang, C. H. Chang, and Y. N. Sun. Registration-Based Segmentation of Three-Dimensional Ultrasound Images for Quantitative Measurement of Fetal Craniofacial Structure. *Ultrasound Med Biol*, 38:811–823, 2012.
- F. Chollet and et al. Keras, 2015. URL https://github.com/fchollet/keras.
- A. V. Dalca, G. Balakrishnan, J. Guttag, and M.R. Sabuncu. Unsupervised learning of probabilistic diffeomorphic registration for images and surfaces. *Med Image Anal*, 57: 226–236, 2019.
- B. D. de Vos, F. F. Berendsen, M. A. Viergever, H. Sokooti, M. Staring, and I. Išgum. A deep learning framework for unsupervised affine and deformable image registration. *Med Image Anal*, 52:128–143, 2019.
- F. Dice and R. Lee. Measures of the amount of ecologic association between species. *Ecology*, 26(3):297–302, 1945.
- Z. Ding, X. Han, and M. Niethammer. Votenet: A deep learning label fusion method for multi-atlas segmentation. In *Medical Image Computing and Computer Assisted Intervention MICCAI 2019*, pages 202–210, 2019.
- L. Fang, L. Zhang, D. Nie, X. Cao, I. Rekik, S. W. Lee, H. He, and D. Shen. Automatic brain labeling via multi-atlas guided fully convolutional networks. *Med Image Anal*, 51: 157–168, 2019.
- B. Gutiérrez-Becker, C.F. Arámbula, H.M.E. Guzmán, J.A. Benavides-Serralde, L. Camargo-Marín, and B.V. Medina. Automatic segmentation of the fetal cerebellum on ultrasound volumes, using a 3d statistical shape model. *Med Biol Eng Comput*, 51(9): 1021–30, 2013.
- J. E. Iglesias and M. R. Sabuncu. Multi-atlas segmentation of biomedical images: A survey. Med Image Anal, 24:205–219, 2015.
- M. Kuklisova-Murgasova, A. Cifor, R. Napolitano, A. Papageorghiou, G. Quaghebeur, M.A. Rutherford, J.V. Hajnal, J.A. Noble, and J.A. Schnabel. Registration of 3D fetal neurosonography and MRI. *Med Image Anal*, 17:1137–1150, 2013.

- H.W. Lee, M.R. Sabuncu, and A.V. Dalca. Few Labeled Atlases are Necessary for Deep-Learning-Based Segmentation. 2019. URL http://arxiv.org/abs/1908.04466.
- A.I.L. Namburete, W. Xie, M. Yaqub, A. Zisserman, and J.A. Noble. Fully-automated alignment of 3D fetal brain ultrasound to a canonical reference space using multi-task learning. *Med Image Anal*, 46:1–14, 2018.
- K. Oishi, L. Chang, and H. Huang. Baby brain atlases. NeuroImage, 185:865–880, 2019.
- M. Rousian, W. C. Hop, A. H.J. Koning, P. J. Van Der Spek, N. Exalto, and E. A.P. Steegers. First trimester brain ventricle fluid and embryonic volumes measured by three-dimensional ultrasound with the use of I-Space virtual reality. *Hum Reprod*, 28:1181–9, 2013.
- M. Rousian, A.H.J. Koning, M.P.H. Koster, E.A.P. Steegers, A.G.M.G.J. Mulders, and R.P.M. Steegers-Theunissen. Virtual reality imaging techniques in the study of embryonic and early placental health. *Placenta*, 64:S29–S35, 2018.
- M. Rousian, S. Schoenmakers, A.J. Eggink, D.V. Gootjes, A.H.J. Koning, M.P.H. Koster, A.G.M.G.J. Mulders, E.B. Baart, I.K.M. Reiss, J.S.E. Laven, E.A.P. Steegers, and R.P.M. Steegers-Theunissen. Cohort Profile Update: the Rotterdam Periconceptional Cohort and embryonic and fetal measurements using 3D ultrasound and virtual reality techniques. *Int J Epidemiol*, pages 1–14, 2021.
- H. Ryou, M. Yaqub, A. Cavallaro, F. Roseman, A. Papageorghiou, and J.A. Noble. Automated 3d ultrasound biometry planes extraction for first trimester fetal assessment. pages 196 204, 2016.
- L.J. Salomon, Z. Alfirevic, C.M. Bilardo, G.E. Chalouhi, T. Ghi, K.O. Kagan, T.K. Lau, A.T. Papageorghiou, N.J. Raine-Fenning, J. Stirnemann, S. Suresh, A. Tabor, I.E. Timor-Tritsch, A. Toi, and G. Yeo. Isuog practice guidelines: performance of first-trimester fetal ultrasound scan. *Ultrasound Obstet Gynecol*, 41(1):102–113, 2013.
- L. Shengfeng, W. Yi, Y. Xin, L. Baiying, L. Li, X.L. Shawn, N. Dong, and W. Tianfu. Deep Learning in Medical Ultrasound Analysis: A Review. *Engineering*, 5:261–275, 2019.
- R.P. Steegers-Theunissen, J.J. Verheijden-Paulissen, M.F. van Uitert E.M., Wildhagen, N. Exalto, Koning A.H., Eggink A.J., Duvekot J.J., Laven J.S., D. Tibboel, I. Reiss, and E.A. Steegers. Cohort profile: The rotterdam periconceptional cohort (predict study). *Int J Epidemiol*, 45:374–381, 2016.
- R.P.M. Steegers-Theunissen, J. Twigt, V. Pestinger, and K.D. Sinclair. The periconceptional period, reproduction and long-term health of offspring: the importance of one-carbon metabolism. *Hum Reprod Update*, 19(6):640–655, 2013.
- J. Torrents-Barrena, G. Piella, N. Masoller, and E. Gratacós. Segmentation and classification in MRI and US fetal imaging: Recent trends and future prospects. *Med Image Anal*, 51:61–88, 2019.

- M. Yaqub, R. Cuingnet, R. Napolitano, D. Roundhill, A. Papageorghiou, R. Ardon, and J.A. Noble. Volumetric segmentation of key fetal brain structures in 3d ultrasound. *International Workshop on Machine Learning in Medical Imaging*, pages 25 32, 2013.
- M. Yaqub, B. Kelly, A. T. Papageorghiou, and J. A. Noble. Guided random forests for identification of key fetal anatomy and image categorization in ultrasound scans. pages $687-694,\,2015.$
- S. Zhengyang, H. Xu, X. Zhenlin, and M. Niethammer. Networks for joint affine and non-parametric image registration. 2019. URL http://arxiv.org/abs/1903.08811.